xxxx

M. P. Arciniegas,* A. Castelli, S. Piazza, S. Dogan, L. Ceseracciu, R. Krahne, M. Duocastella, L. Manna* .....x–xx

Laser-Induced Localized Growth of Methylammonium Lead Halide Perovskite Nano- and Microcrystals on Substrates

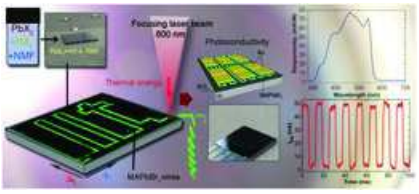

Stable $MAPbBr_3$ crystals with different sizes are successfully localized on a flat substrate via laser-induced heating of the liquid precursors. By adjusting the infrared laser parameters, luminescent arrays and photoconductive wires are grown on-site. This technique can be used to guide the writing of other patterns for specific functionalities.

ADVANCED FUNCTIONAL MATERIALS

xxxx

www.afm-journal.de

Laser-Induced Localized Growth of Methylammonium Lead Halide Perovskite Nano- and Microcrystals on Substrates

Milena P. Arciniegas, Andrea Castelli, Simonluca Piazza, Sedat Dogan, Luca Ceseracciu, Roman Krahne, Marti Duocastella, and Liberato Manna**

Perovskite-based optoelectronic devices have shown remarkable performances, especially in the field of photovoltaics. Still, a rapid solution processing approach able to produce localized stable perovskite crystals remains a general challenge and is a key step toward the miniaturization of such materials in on-chip components. This study presents the confined growth of methylammonium (MA) lead halide perovskite crystals that are thermally induced through a localized laser irradiation. Importantly, such structures remain stable over time, that is, they neither dissolve back into the surrounding liquid nor detach from the substrate. This is attributed to a chemical reaction locally triggered by the induced heat on the substrate surface that is transferred to the perovskite precursors (liquid) layer, thus generating "on-demand" MA ions from the *N*-methylformamide solvent. By tuning the laser parameters, such as power density or irradiation time, variations in shape and size of the crystals, from microcrystals of ≈50 µm to nanocuboids of ≈500 nm are observed. This study also demonstrates that, with an optimized distance between the irradiated regions and by controlling the relative laser displacement speed, luminescent and photoconductive $MAPbBr_3$ wires and microplates can be generated.

1. Introduction

The extremely versatile properties exhibited by halide perovskites-based systems have made them among the most studied in the field of optoelectronics in the last years.[1–4] Thanks to their tunable bandgap,[5,6] high charge-carrier mobility[7] and high photoluminescence quantum yield,[8] along with the possibility of adjusting such features by simple replacement of the cation(s) or halide component,[9–11] halide perovskites have emerged as attractive low-cost alternative materials suitable for many technologies. Their easy solution-processability has also facilitated their direct integration in devices such as photodetectors,[12,13] light emitting diodes,[10,14] and solar cells,[15,16] where they have reached competitive performances.

Methylammonium (MA) lead halide perovskites, especially $CH_3NH_3PbX_3$ (X = Cl, Br, I), have been extensively studied in the form of bulk crystals,[17,18] thin films,[19,20] and nanocrystals,[21,22] and several different routes are being explored to fabricate high quality materials. It is also known that the way perovskite precursors are processed has a strong impact on the performance of the resulting materials, in particular for the preparation of thin films.[23,24] Typically, thermal treatments following conventional solution-processing strategies are required to enhance their energy conversion efficiency in solar cells and to accelerate their crystallization from the solution phase, for a less expensive and rapid preparation.[25–28] In general, the developed approaches involve multiple steps, from the preparation of the

M. P. Arciniegas, A. Castelli, S. Dogan, R. Krahne, L. Manna
Nanochemistry Department
Istituto Italiano di Tecnologia
Via Morego 30 Genova, 16163, Italy
A. Castelli
Dipartimento di Chimica e Chimica Industriale
Università degli Studi di Genova
Via Dodecaneso, 31 Genova, 16146, Italy
S. Piazza, M. Duocastella
Nanoscopy and NIC@IIT
Istituto Italiano di Tecnologia
Via Morego 30 Genova, 16163, Italy
S. Piazza
Dipartimento di Informatica
Bioingegneria
Robotica ed Ingegneria dei Sistemi
Università degli Studi di Genova
Via Opera Pia 13 Genova, 16145, Italy
L. Ceseracciu
Materials Characterization Facility
Istituto Italiano di Tecnologia
Via Morego 30 Genova, 16163, Italy
Correspondence to: M. P. Arciniegas (E-mail: milena.arciniegas@iit.it), L. Manna (E-mail: liberato.manna@iit.it)

DOI: 10.1002/adfm.201701613

MA salts to the selection of the deposition technique related to the device fabrication steps.[29–32] Despite the notable advantages of the solution processing methods, the poor stability of $MAPbX_3$ perovskites in conventional solvents and the growth of intermediate phases during dewetting of deposited precursors make it difficult to control their crystallization properly.[29, 33, 34] These issues become relevant in the cases where precise localization of the nucleation spots is needed, which is crucial for creating ordered arrays of perovskite crystals directly from the liquid phase. There are few examples of local growth of periodic arrays of $MAPbX_3$ perovskites, and primary for the $MAPbI_3$ system. These are seeded growth of microplates,[35] growth of nanoplatelets by physical vapor deposition on prefabricated 2D substrates,[36] growth of nanowires guided by nanofluidic channels,[37] and dewetting control of the precursor solution by "liquid knife."[38] Recently, a more direct approach has been implemented through the use of a near-infrared laser as the energy source to induce the perovskite conversion from a mixture of MAI with PbI_2 in gamma-butyrolactone and dimethyl sulfoxide solvents that provides uniform $MAPbI_3$ thin films for photovoltaics.[39] This route has been later explored to nucleate on-site $MAPbBr_3$ microcrystals for photodetectors from a solution of MABr with $PbBr_2$ in dimethylformamide.[40] This latter work evidenced the remarkable advantages that the laser techniques bring to the processing of such materials, for example a reduced processing time and controlled positioning of the perovskite structure in the desired regions, without the need of masks or multiple lithography steps. On the other hand, if a more robust and reliable laser protocol could be followed, it would be possible to overcome issues such as poor stability and limited size control of the locally generated perovskite crystals.

In this work, we describe the capability of a system based on a solution of PbX_2 in HX with *N*-methylformamide (NMF) to locally crystalize stable $MAPbX_3$ structures on a flat substrate when exposed to the infrared radiation from a laser, at room temperature. The approach employs low-toxicity perovskite precursors that can deliver MA ions through the acid-catalyzed hydrolysis of NMF.[41] This reaction is enhanced locally by the laser-induced thermal energy on the substrate, which is transferred to the liquid precursor layer. Under suitable experimental conditions, the spontaneous formation of MA ions did not occur in the absence of near-infrared irradiation (for the time scale of the experiments) and, instead, was triggered by the laser. This induced a localized nucleation, which was then controlled by adjusting the laser parameters, such that different geometries (arrays of dots, squares, and wires) could be written on the substrate in seconds.

2. Results and Discussion

In our experiments, we prepared a fresh solution of perovskite precursors containing $PbBr_2$ (1 M concentration) in 60 µL of HBr and 350 µL of NMF, following the procedure described for the growth of $MAPbBr_3$ bulk crystals in a recent work from our group.[41] Prior to the deposition of the precursor solutions, the Si substrates were mounted on the laser sample holder of the motorized stage to focus the objective lens on their top surface. Then, we placed an aliquot (0.2 µL) of the perovskite precursor

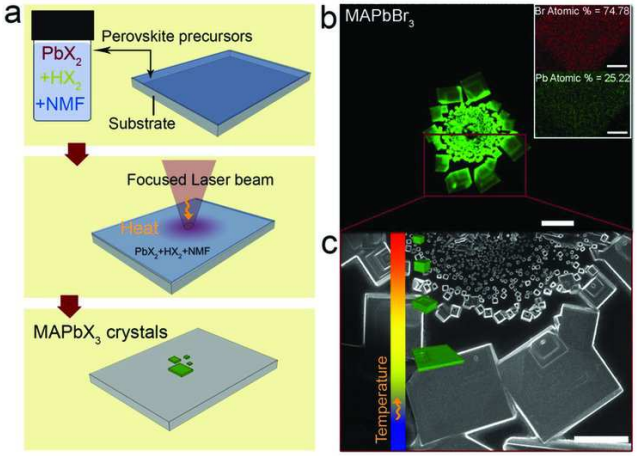

Figure 1. Laser-induced nucleation of $MAPbX_3$ crystals. a) Sketch of the laser-printing process: the mixture of perovskite precursors is deposited on a Si substrate that is irradiated with an 800 nm laser. In the beam focused region a heat distribution is induced, promoting the formation of $MAPbX_3$ crystals; b,c) Fluorescence and SEM correlative images of the $MAPbBr_3$ crystals taken shortly after laser irradiation. Scale bars, 100 and 50 µm, respectively; the inset in b) shows the EDS analysis of a representative crystal that confirms their Pb:Br atomic ratio of 1:3, supportive of the perovskite structure. Scale bars: 2 µm. The embedded cartoon illustrates the size dependence of the crystals with the laser (radial) induced temperature in the spot, from the coldest regions in blue to the hottest ones in red.

solution on the substrates, allowing it to spread over the surface for a few minutes, such that a thin and uniform liquid layer over several square millimeters was formed (**Figure 1**a). We used a femtosecond laser at 800 nm wavelength with a repetition rate of 80 MHz and average power ranging from 180 to 370 mW to induce the local heating of the substrates necessary to promote the nucleation and growth of perovskite crystals (see Experimental Section and Table S1 of the Supporting Information for details). Note that all the as-deposited solutions of perovskite precursors are transparent to the laser wavelength, as confirmed by their absorption spectra (see Figure S1 of the Supporting Information). Thus, the light is only absorbed by the substrate, which then generates heat that is dissipated to the liquid layer above,[42] as illustrated in Figure 1a. This laser-induced local temperature gradient is what leads to the formation of perovskite crystals on specific sites on irradiated planar substrates (see a scheme of the process in Figure S2 of the Supporting Information). Typically, the sample dries during the fabrication process, and the obtained perovskite crystal structures can be inspected immediately after their fabrication by fluorescent microscopy with low-power excitation in the UV/blue (both in the same setup used for the laser-printing, and in other more standard confocal fluorescent microscopes). Furthermore, we investigated the samples by scanning electron microscopy (SEM) in order to analyze the size and shape of the crystals at higher resolution.

First, we demonstrate the feasibility of our method to grow stable perovskite crystals with controlled size on targeted locations on the Si substrate. To this end, we irradiated the liquid layer of the $MAPbBr_3$ perovskite precursors at fixed positions with the laser focused on a spot size of 12 µm diameter (0.5 s

of exposure). Figure 1b shows a fluorescent image (excitation at 430 nm, detection band 535–550 nm) that was recorded shortly after the laser exposure, where we observe a small central void region that is surrounded by an inner ring of small (few 100 nm sized) nanocrystals, and an outer ring of micrometer-sized rectangular sheets. The SEM image in Figure 1c, taken from the same region, demonstrates the stability of the fabricated crystals; they preserve their shape and remain attached to the substrate surface. Careful comparison of the confocal and SEM images shows that the microcrystals in the outer ring have undergone an additional overgrowth of ≈10%, while for the ones in the central ring we do not observe a change in size. Importantly, the crystals were only formed in a well-defined localized region around the laser spot, i.e., no spontaneous growth at arbitrary locations was observed. Elemental analysis via energy dispersive spectroscopy (EDS) of the fabricated structures (in the scanning electron microscope) for Pb and Br indicates a 1:3 atomic ratio (Figure S3, Supporting Information). This confirms the formation of $MAPbBr_3$ perovskite crystals, as also evidenced by the X-ray diffraction (XRD) patterns (Figure S16, Supporting Information). Our data point to a process where acid-catalyzed hydrolysis of the NMF in solution[41] is driven by the laser-induced heating, which results in the on-demand formation of MA ions by the precursors and leads to the local formation of stable $MAPbBr_3$ perovskite crystals.

A detailed analysis of the laser-induced $MAPbBr_3$ crystals shows that several fully developed crystals with a cubic shape and a lateral size of less than 2 μm nucleate in the inner region, where the temperature should be highest. Also, fewer larger structures appear further away from the irradiated spot, indicating an increase in perovskite crystal size with decreasing laser-induced temperature. We observed structures up to 25 μm crystalizing in an intermediate region, followed by a more abrupt change to significantly larger plate-like crystals with a lateral size up to 100 μm and a thickness of ≈2 μm that constitute the outer ring of the deposit (see closer views in Figure S4 of the Supporting Information). These observations indicate that the formation of the laser-induced crystals follows a classical nucleation-driven growth mechanism that typically depends on the temperature of the system: at high temperatures more nuclei are formed with less precursors available and thus smaller structures grow (inner region), while fewer nuclei are induced at lower temperatures, promoting larger crystals. A theoretical evaluation of the laser-induced temperature on the Si substrate shows that it reaches ≈110 °C in the center of the irradiated spot and that the temperature decreases to ≈60 °C at a distance of 5 μm after 30 ms of laser irradiation (see Figure S5 in Section III of the Supporting Information). Further evidence of the conversion of the absorbed laser energy into heat comes from thermal images of the Si substrates acquired before and after laser irradiation (see Figure S6 in the Supporting Information). Moreover, in our system, the laser-induced thermal gradient strongly influences the local concentration of precursors, since the formation of MA ions in the irradiated region is enhanced by the generated thermal energy. The local variation in the concentration of MA ions is most likely responsible for the screw-dislocation growth observed in individual crystals located in the low-temperature regions, as evidenced by the spiral characteristic feature of this mechanism (see closer SEM images in the right panel of Figure S4 of the Supporting Information).[43,44] Hence, the extent of laser-induced temperature gradient can be used to control the size and morphology of perovskite crystals in our fabrication process.

We now analyze in detail the influence of the laser irradiation dose (at fixed power of 370 mW) on the resulting induced perovskite crystals. Since the fabrication of crystals with the laser is strongly influenced by the acid-catalyzed hydrolysis of the NMF in solution, we first tested the responsivity to the laser irradiation of the perovskite precursors after different times of incubations at ambient temperature (22 °C); see Table S1 and Figure S7 of the Supporting Information. We found that the solution incubated for 1 h requires significantly higher irradiation doses for the formation of perovskite crystals. At 2.3×10^7 and 4.8×10^7 J cm^{-2} (that correspond to 10 and 21 s of exposure time at 370 mW), we observed very few detached cuboid structures of ≈15 μm; at even higher irradiation doses (9.7×10^7 J cm^{-2}, 42 s of exposure time), concentric small structures were formed with a significant overgrowth in the outer region (see Figure S7 of the Supporting Information). With a longer incubation time (6 h) of the solution, the irradiation dose needed for the crystal formation is significantly reduced. In this case, a donut-shaped region of crystals with sizes of approximately 25 μm is already formed at a dose of 1.1×10^7 J cm^{-2} (corresponding to 5 s exposure time), and increasing the irradiation dose up to 4.8×10^7 J cm^{-2} more defined plate-like crystals are observed (see the first panel in **Figure 2**a). This higher reactivity of the perovskite precursors with the incubation time can be explained by the increased release of MA ions in the solution over time from the slow acid hydrolysis of NMF in the presence of HX.[41] The 6 h incubation solution also enables to clarify the effect of the irradiation dose (and therefore laser-induced heating) on crystal formation: At relatively low doses (4.8×10^7 J cm^{-2}, lower laser-induced temperature), few nuclei are formed that are fed by MA ions from the surrounding liquid, which favors formation of a smaller number of crystals with a large dimension (see Movie S1 recorded at 40 frames s^{-1}, and snapshots in Figure S8 of the Supporting Information). In contrast, by increasing the irradiation dose to 9.7×10^7 J cm^{-2} (exposure time of 42 s), the higher temperature induces a larger number of nucleation points and the competition for the available perovskite precursors becomes harder, resulting in the formation of smaller structures with a cubic shape that are randomly distributed in the vicinity of the irradiation spot (see red-framed panel in Figure 2a). A closer view of the $MAPbBr_3$ crystals that were formed under these low and high irradiation doses of 4.8×10^7 and 9.7×10^7 J cm^{-2} can be appreciated in Figure S9 of the Supporting Information. We also tested higher laser irradiation doses, ranging from $\approx 14 \times 10^7$ to 42×10^7 J cm^{-2} (corresponding to exposure times of 60 s to 3 min), to check if such conditions could help to localize smaller structures from the 6 h incubated precursors. Interestingly, we found that macroscopic 3D dome-shaped structures grew in the irradiated spots at such high irradiation doses (see fluorescence images in Figure S10 of the Supporting Information); these domes are composed by smaller green-emitting crystals with a Pb:Br atomic radio near 1:3, as confirmed by EDS (see Figure S11 of the Supporting Information). This aggregation of crystals can be explained by the high temperature gradient induced in the liquid layer that promotes vigorous radial convective fluxes: a

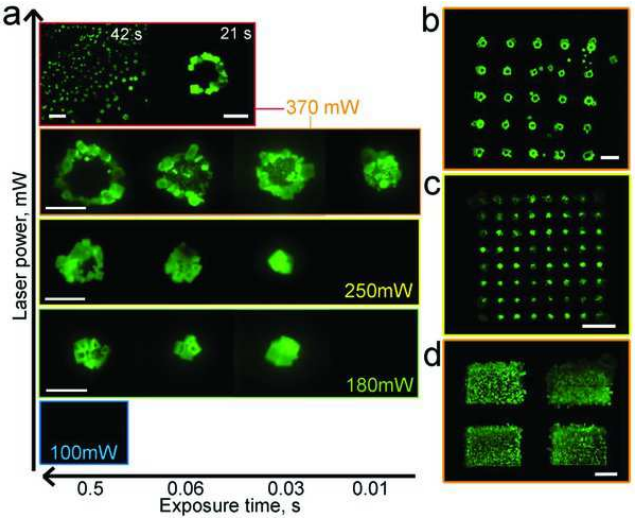

Figure 2. a) Colored fluorescence images taken after laser irradiation, evidencing the changes on size and distribution of the induced $MAPbBr_3$ crystals by variation on the laser power and the exposure time: Plate-like structures up to 25 μm form at high power in a donut shape; while very few compact and smaller platelets grow around the irradiated region at reduced laser power (less than 250 mW). Below 180 mW no laser-induced crystal growth occurs. The color of the image frames from red to blue illustrates the induced temperature, from high to low, with each laser power. Note that at 370 mW cuboids of 500 nm to 2 μm grow randomly dispersed after higher irradiation doses (42 s). Scale bars in blue to orange panels: 50 um; Scale bars in the red framed panels: 5 μm (left) and 50 μm (right). b,c) 5 × 5 and 8 × 8 arrays of $MAPbBr_3$ plates for arrays with spacing of b) 150 μm and c) 50 μm. For (b) and (c), laser powers of 370 and 250 mW were used. Scale bars: 100 μm. d) Arrays of 2 × 2 rectangles spaced 100 μm. Scale bar: 100 μm.

driving force that collects and locates the perovskite structures in a central point. This mechanism can be of use for laser-printing 3D geometries made of perovskite crystals.

We observed that irradiation of a single spot typically resulted in a donut-shaped distribution of the $MaPbBr_3$ crystals on the substrate surface that could only be avoided at very low irradiation doses (see Figure 2a). The depletion of material in the center of the donut may be explained by two different phenomena: (i) the temperature at the center could be too high for proper crystal growth to occur; and (ii) it is likely that there is an induced convective flux from the center toward the periphery of the irradiated area that displaces the crystals accordingly. Therefore, we tested lower irradiation doses to tune the crystal size and to achieve crystal growth also in the center of the heated region, and thus to obtain, in principle, a single crystal in the irradiated region. To this end, we used the 6 h incubated solution and varied both the laser power and the exposure time. Figure 2a shows a series of fluorescent images taken after irradiating the precursor layer at 100, 180, 250, and 370 mW for different laser exposure times/irradiation doses (see details in Table S3 of the Supporting Information).

At high laser powers, the donut-like distribution of perovskite crystals dominates in the growth region. A lower irradiation dose leads to a smaller area in which the crystals are formed (laser-activated spot). For example, at laser powers of 250 and 180 mW and short exposure times, we achieve well-compacted perovskite structures. The average size of the crystals formed under different laser exposure conditions is reported in Table S2 of the Supporting Information, and Figure S12 of the Supporting Information shows how the size of the laser-activated spot can be controlled by the irradiation dose. The proper optimization of such parameters can potentially lead to the localized growth of individual crystals in an irradiated region below 50 μm.

With the point-by-point exposure, regular arrays of perovskite crystal deposits can be fabricated. Figure 2b shows an array of donuts with pitch of 150 μm printed with a laser power of 370 mW, where we observe the occasional formation of crystals far away from the irradiated regions. Interestingly, we found a dependence of the array pitch d on whether or not crystals are formed at random position or solely near the irradiated spots. That is, if the pitch is reduced to 50 μm (keeping the other writing parameters fixed), we observe only the formation of crystals at positions that correspond to the array pattern as demonstrated in Figure S13 of the Supporting Information. This effect can be rationalized considering that, for smaller pitch, less volume of precursors is available to feed the crystal growth in the irradiated region for each single shot. Therefore the precursors get fully consumed by the growing crystals, leaving no material for spurious floating nuclei to grow (as observed when working at low laser power). Using a pitch of 50 μm and 250 mW leads to an optimized array of perovskite crystals with almost circular deposits and no deposits in between the shots. Figure 2d shows rectangular regions consisting of submicrometer-sized crystals that can be achieved by laser scanning on these regions (at 370 mW). Here too, we observed no formation of extra deposits for smaller distance (≈100 μm) between the rectangles, while, for large distance (≈400 μm) between the elements, extra growth at undesired positions can occur (see Figure S13 of the Supporting Information).

The versatility of our method can be extended by the continuous printing of perovskite crystal structures with a relative moving laser beam over the substrate surface that allows for the fabrication of larger structures, for example wires with millimeter-scale length (Movie S2 of the Supporting Information). We realized that by keeping the laser beam fixed and moving the stage at velocities of few mm s^{-1}, and we obtained continuous wires consisting of aggregated perovskite crystals when working with a constant laser power of 370 mW. In this approach, the formation of the $MAPbBr_3$ crystals depends strongly on the relative velocity of the laser beam, as can be seen in **Figure 3**a.

At low velocities (0.5 and 1 mm s^{-1}), we observe the formation not only of the wires along the irradiated lines but also of a large number of crystals in the surrounding area. The best condition for continuous wire fabrication is found at a velocity of 1.5–2 mm s^{-1}, where the crystal formation is occurring solely along the exposed lines, and robust wires with a width of around 20–30 μm are formed (by crystals of ≈25 μm^2, see Figure S14 of the Supporting Information). Higher velocities lead to isolated large crystals and therefore discontinuous lines. The difference in relative laser velocities results in a different extension of the heat distribution around the exposed line, which in turn affects the amount of precursors that is involved in the reaction (see defects on Figure S15 of the Supporting Information). Low velocities lead to a broad heat distribution, and therefore also to

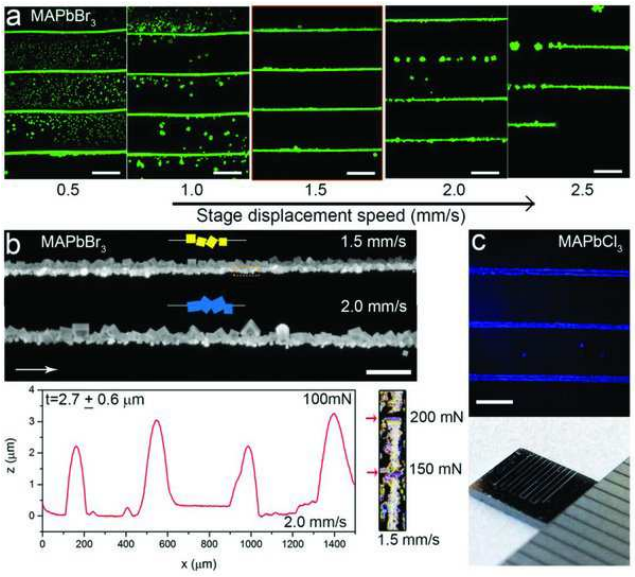

Figure 3. a) Colored fluorescence images of the $MAPbBr_3$ wires prepared under different stage displacement speeds. b) (Top) Unprocessed fluorescent closer views of wires produced at 1.5 and 2.0 mm s^{-1}. Scale bars: 100 μm The white arrow indicates the direction of the relative laser displacement and the embedded sketches highlight the organization of crystals in the wires. (Bottom) Transverse profile of a set of four wires prepared at 2.0 mm s^{-1} showing a thickness (t) of ≈3 μm, a higher value with respect to the one found for a similar set with a speed of 1.5 mm s^{-1} ($t = 1.2 \pm 0.5$ μm). c) Colored fluorescence image showing a set of three $MAPbCl_3$ wires prepared at 1.5 mm s^{-1}. Scale bars in (a) and (c): 200 μm.

nucleation points further away from the irradiated region (as observed for 0.5 mm s^{-1} in Figure 3a). On the other hand, at higher velocities (1.5–2 mm s^{-1}) the laser-induced heat distribution is significantly narrower and the threshold for the crystal nucleation is restricted close to the exposed line. Increasing the velocity further leads first to isolated nucleation along the exposed line, and at even higher velocities (2.5 mm s^{-1}) the laser provided heat is not anymore sufficient to induce nucleation. The typical height of the continuous wires is a few micrometers as is shown in Figure 3c by low-force (30 mN) scratches. The robustness of the wires is demonstrated by line scans under high tip load values that proved resistance up to 150 mN. Comparison between XRD data collected from these wires and a powder of bulk $MAPbBr_3$ crystal corroborates the conversion of the irradiated precursors to a cubic $MAPbBr_3$ crystal phase (Figure S16, Supporting Information). The crystal structure is not affected by a posttreatment that consisted in a vertical immersion of the substrates in acetone to remove the excess of perovskite precursors deposited on the substrates (see Figure S16 of the Supporting Information). Such stability has already been observed in perovskite crystals prepared by other protocols.[45,46] The crystals exhibit a photoluminescence peak at ≈540 nm (see Figure S17 of the Supporting Information) that is typical of this type of $MAPbBr_3$ microcrystals.[47,48] We extended our approach for wire fabrication to other NMF/HX-based precursors to induce the formation of $MAPbCl_3$ and $MAPbI_3$ crystals, which showed promising results (Figure 3c; Figure S18, Supporting Information), although for these materials the laser parameters need further optimization.

$MAPbBr_3$ microcrystals and continuous wires of such crystals can be interesting for optoelectronic devices and therefore we investigated their (photo)conductive properties. To this end, we followed two approaches: (i) the $MAPbBr_3$ wires were fabricated prior to the electrical contacts on 100 nm SiO_2-coated Si substrates and then contacted by shadow mask evaporation with gold electrodes (4 nm Ti + 50 nm Au), as illustrated in the top panel of **Figure 4**a; and (ii) the $MAPbBr_3$ microcrystals were selectively laser-grown in the gap (≈10 μm) of prefabricated electrode pairs (bottom panel in Figure 4a). These two possibilities highlight the flexibility of our approach that allows to control the position and to some extent also the size and shape of the perovskite structures. The SEM images in Figure 4a show a closer view of a gold electrode evaporated on top of a laser-induced $MAPbBr_3$ wire (approach (i)); and a laser-induced $MAPbBr_3$ microplate (size ≈20 × 20 μm^2) bridging two Au electrodes, as described in the approach (ii). The illumination power-dependent I–V characteristics of such $MAPbBr_3$ wires and microplate recorded at a fixed laser wavelength of 473 nm (above the bandgap of $MAPbBr_3$) and in dark conditions are shown in Figure 4b (microplate) and Figure S19 (wires) of the Supporting Information. In the dark, the conductance of the wires and microplate is negligible, with only few pA at a bias of several volts (black line). Under illumination, the I–V manifests hysteresis with respect to the direction of the voltage sweep, and a strongly nonlinear behavior (see I–V curves in Figure S20 of the Supporting Information). In the case of the wires, the photo I–V in the range from 0 to 5 V can be described by the empirical cold-field emission model[49] that has been successfully applied to the photocurrent in nanocrystal assemblies,[50] and the current can be fitted by $I(V) = CV^{\kappa}\exp(-B/V)$, where C, κ, and B are constants (see Figure S21 of the Supporting Information).

The photocurrent scales approximately linearly with the laser power in both cases (inset of Figure 4b; Figure S19a, Supporting Information). We observe from the wires a slightly superlinear dependence of the photocurrent on incident laser power that could be related to slightly reduced tunnel barriers at high carrier density, which is in agreement with the cold-field emission model. We tested the response time of the photocurrent for both approaches described above by switching the illumination on and off at a frequency of 80 Hz and a power intensity of 100 mW cm^{-2}, which translates to a regular photocurrent pattern (Figure 4c), from which a rise time of 1.0 ms and a fall time of 1.1 ms can be extracted (Figure 4e). These values are in line with those reported for MA lead iodide perovskites photodetectors.[41] The spectral photoresponsivity of the microplates, recorded under illumination with a Xenon lamp coupled to a monochromator (see details in the Experimental Section) at a fixed voltage of +3V is reported in Figure 4d. On the long wavelength side, the spectrum shows a sharp onset at 580 nm (≈2.13 eV) and a peak at 540 nm, which reflects the band-edge absorption of the $MAPbBr_3$ crystals (see Figure S22 of the Supporting Information).[26] In the range from 500 to 400 nm, the responsivity remains high with a maximum value of 0.83 mA W^{-1} and decreases toward the UV region due to increased trapping of high-energy photoexcited carriers in surface and defect traps.[51,52] The results obtained from the

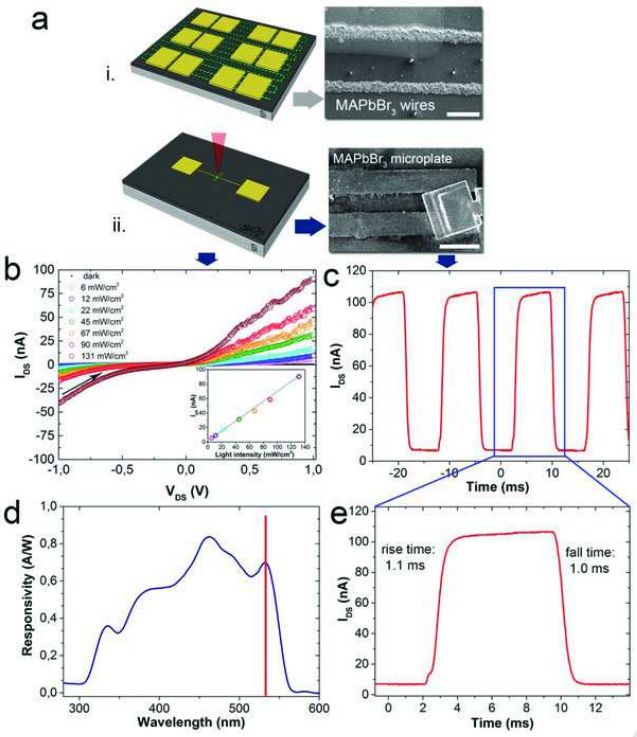

Figure 4. Optoelectronic properties of the laser-induced microplates and wires consisting of $MAPbBr_3$ crystals. a) Scheme of the device configurations used to evaluate the different responses of the microplate and wires. The SEM images show a wire after the top Au electrodes deposition and a stacked perovskite microplate bridging prefabricated Au electrodes with a gap of 10 μm. Scale bars: 50 μm (top) and 20 μm (bottom). b) *I–V* curves in the dark and upon illumination at different light power. The inset shows the photocurrent as a function of the applied light power at a bias of 1 V. c,e) Temporal photoresponse of the microplate when switching the illumination on and off. d) Normalized photocurrent spectrum recorded at a bias voltage of 3 V. The red line highlights the peak maximum at 540 nm.

wires fabricated along approach (i) are reported in Figure S19 of the Supporting Information.

3. Conclusions

In summary, we have demonstrated the spatially localized growth of perovskite crystals with different size, ranging from the nanometer to the micrometer scale, on different substrates via laser-induced heating of liquid precursors. This method enables direct nucleation and on-site growth of stable $MAPbX_3$ crystals at specific locations or in functional patterns by using laser sources that are commonly available. Furthermore, it has the additional advantage that immediate inspection of the obtained structures by conventional fluorescence microscopy can be easily implemented. We demonstrate the potential of this process for optoelectronic applications by writing luminescent arrays and photoconductive wires on planar substrates. The direct fabrication of functional structures by laser writing that we show provides several advantages that are highly relevant for device fabrication: (i) no extra lithography steps are needed to obtain patterned structures; (ii) the pattern, and the perovskite crystal size and shape that constitute it, can be controlled in situ and customized to specific needs; and (iii) the process uses a significantly lower amount of resources to obtain functional optoelectronic structures as compared to, for example, spin coating or liquid knife deposition techniques of perovskite inks (that additionally need to be combined with lithography processes).

4. Experimental Section

Chemicals: Lead (II) bromide ($PbBr_2$, 99.999%), lead (II) iodide (PbI_2, 99.999%), hydrobromic acid (HBr, 48% in mass in water), hydrochloric acid (HCl, ACS reagent, ≥37% in mass in water), hydriodic acid (HI, 99.99%), and NMF (99%) were purchased by Sigma-Aldrich. Lead (II) chloride ($PbCl_2$, 99%) was purchased from Strem Chemicals. All reagents were employed as received.

Solution and Sample Preparation: The mixture of $MAPbBr_3$ perovskite precursors (1 M concentration) was prepared with $PbBr_2$ (150 mg) in HBr (60 μL) and NMF (350 μL). The solution of $MAPbCl_3$ perovskite precursors (0.2 M) was prepared with $PbCl_2$ (111 mg of $PbCl_2$) in HCl (200 μL) and NMF (1.800 mL). Finally, the solution of $MAPbI_3$ perovskite precursors was prepared by using HI (670 μL) and NMF (670 μL) and added them to PbI_2 (378 mg). All the mixtures were sonicated for 10 min to obtain a limpid solution. P-type Si substrates purchased from Ted Pella were used as laser absorbing supports with sizes of 5×5 mm² and 12×16 mm². Prior to solution deposition all the substrates were cleaned via sonication (5 min) in acetone, distilled water, and isopropanol and dried with compressed air. The surfaces were then exposed to a plasma treatment (Gambetti Tucano Multipurpose Plasma System) with O_2 flow for 5 min at 150 W. Finally, the substrates were fixed on glass slides with a double face adhesive tape that was carefully mounted on the laser stage, and an aliquot (0.2 μL) of perovskite precursors were deposited on the top of the silicon substrates, and after 10 min the sample was ready for laser irradiation. A complete list of the laser parameters used is given in Tables S1 and S3 of the Supporting Information.

Laser Setup: All experiments were performed using a Ti:sapphire femtosecond laser operating at 800 nm (Chameleon, Coherent GmbH, rep. rate: 80 MHz, pulse width: <140 fs). A commercial scanning microscope (Confocal C2, Nikon) equipped with a long working distance objective lens (10×, NA = 0.28, WD = 33.5 mm, Mitutoyo) was used to focus light on the silicon substrate. 1D patterns including dot arrays and lines were obtained by moving the sample in the *XY* plane with a motorized stage (2 MT1-Z8 linear translation stages, Thorlabs) while keeping the laser beam steady. 2D and 3D structures (e.g., squares) were instead obtained by employing the XY galvo scanner of the microscope in order to scan a preselected area of the silicon substrate. Power of the laser was set at different powers, from 100 to 370 mW, as described in the main text.

Structural and Optical Characterization: XRD analysis was carried out on a Rigaku SmartLab X-ray powder diffractometer equipped with a 9 kW CuKα rotating anode, operating at 40 kV and 150 mA with an aperture of 1 mm. A Göbel mir-

ror was used both to convert the divergent X-ray beam into a parallel beam and to suppress the Cu Kβ radiation. Fluorescent and white light optical microscopy investigation was carried out with a Nikon Eclipse 80i upright fluorescence microscope illuminated with a high-intensity arc lam and equipped with a DAPI filter (ex 360/40, em 460/50 used for $MAPbCl_3$ imaging), an FITC filter (ex 470/30, em 535/50 used for $MAPbBr_3$ imaging), and a TRITC filter (ex 540/25, em 605/25 used for $MAPbI_3$ imaging). The images were collected with a high-speed cooled monochrome CCD camera head DS-SMB Wc. High-resolution SEM analyses were conducted on a FEI Helios NanoLab 600 Dualbeam (FEI/SEM) system. The elemental chemistry analysis was conducted via EDS in a JEOL JSM-7500FA SEM. The photoluminescence spectra were collected on laser irradiated samples with a Horiba FluoroMax 4 spectrometer. The absorption spectra from fresh mixtures of $MAPbX_3$ perovskite precursors and their single liquid components (NMF and HX) were recorded with a Varian Cary 5000 UV–vis–NIR spectrophotometer. An aliquot (50 μL) of the perovskite precursors was deposited on a glass substrate and annealed at 120 °C for 10 min to collect the absorption spectrum shown in Figure S21 of the Supporting information. Scratch tests were performed across sets of $MAPbBr_3$ wires on a CSM MicroCombi system with a 1 mm diameter steel ball at a speed of 1 mm min^{-1} for a total scratch length of 1.5 mm. The tests were conducted with different loads (100, 150, 200, 250, and 300 mN) to determine the critical force to produce removal of crystals from the wires and thus providing a comparative estimation of crystal adhesion to the substrates. Additional scratches at low force (30 mN) were used to determine the wires thickness. To collect thermal images and estimate the average temperature of the Si substrates before and after laser irradiation an infrared Fluke TiR32 Thermal Imager (up to wavelength of 14 000 nm) was used. Theoretical analysis on the temperatures induced by laser cumulative heating on the Si substrate was performed with Matlab.

Optoelectrical Characterization: In the case of the wires, the structures were fabricated by first drawing $MAPbBr_3$ wires on 100 nm thick layer of SiO_2 coating on Si-substrates acquired from Ossila. Next, gold layers (≈50 nm) acting as electrical contacts were deposited on the top of the wires through thermal evaporation by using a shadow mask (arrays spaced 40 μm), after deposition of 5 nm of Ti using the same protocol. In the case of the microplates, the electrodes were defined on *n*-doped Si substrates with a thermal oxide layer of 100 nm by electron beam lithography. For this, the substrates were spin-coated with poly(methyl methacrylate) and the patterning was carried out using the Raith 150-Two NanoSuit software in a SEM microscopy (from Zeiss). After defining the electrodes, 5 nm of Ti and 50 nm of Au were deposited using an electron-beam evaporator. The electrodes were spaced 10 μm. Current–voltage curves were recorded under vacuum using a Janis probe. The photocurrent spectra were acquired using an ASB-XE-175 Xe-light source, which was passing through a CM110 1/8m monochromator to tune the wavelength between 300 and 800 nm. The power spectrum of the Xe-lamp/monochromator was recorded in the same setup using a Thorlabs DET10A silicon photodiode in order to correct the photocurrent spectra. The time-dependent measurements were carried out by using a chopper to modulate the incoming light. The transient photocurrent was then measured using a DSO-X 2014A oscilloscope from Agilent technologies. The risetime is defined as the time needed for the current to rise from 10% to 90% of maximum value and the falltime corresponds to the time that takes for the system to fall 90% to 10% of the maximum current.

Supporting Information

Supporting Information is available from the Wiley Online Library or from the author.

Acknowledgements

The authors acknowledge financial support from European Union through the FP7 consolidator ERC grant Trans-Nano (Contract Number 614897). A.C. and M.P.A. thank S. Lauciello for the technical support on the EDS analysis, S. Marras and S. Accornero for the technical support on XRD, and M. Prato for the useful discussions. M.P.A. and S.D. thank M. Leoncini for the technical support on the device preparation. M.P.A. thanks T. Avellini for the technical support on the acquisition of thermal images. Use of the Materials Characterization Facility @ IIT for XRD and scratch characterization is acknowledged. The manuscript was written through contributions of all authors. All authors have given approval to the final version of the manuscript. The authors declare no competing financial interest.

Q4

Conflict of Interest

The authors declare no conflict of interest.

Keywords

laser, patterning, perovskites, photoconductive wires, thermal crystallization

Received: March 28, 2017
Revised: June 10, 2017
Published Online: MM DD, YYYY

[1] J. S. Manser, J. A. Christians, P. V. Kamat, *Chem. Rev.* **2016**, *116*, 12956.
[2] P. Docampo, T. Bein, *Acc. Chem. Res.* **2016**, *49*, 339.
[3] H. Zhu, Y. Fu, F. Meng, X. Wu, Z. Gong, Q. Ding, M. V. Gustafsson, M. T. Trinh, S. Jin, X. Y. Zhu, *Nat. Mater.* **2015**, *14*, 636.
[4] F. Giustino, H. J. Snaith, *ACS Energy Lett.* **2016**, *1*, 1233.
[5] B. R. Sutherland, E. H. Sargent, *Nat. Photonics* **2016**, *10*, 295.
[6] R. J. Sutton, G. E. Eperon, L. Miranda, E. S. Parrott, B. A. Kamino, J. B. Patel, M. T. Hörantner, M. B. Johnston, A. A. Haghighirad, D. T. Moore, H. J. Snaith, *Adv. Energy Mater.* **2016**, *6*, 1502458.
[7] T. M. Brenner, D. A. Egger, L. Kronik, G. Hodes, D. Cahen, *Nat. Rev. Mater.* **2016**, *1*, 15007.
[8] S. D. Stranks, H. J. Snaith, *Nat. Nanotechnol.* **2015**, *10*, 391.

[9] C. M. Sutter-Fella, Y. Li, M. Amani, J. W. Ager, F. M. Toma, E. Yablonovitch, I. D. Sharp, A. Javey, *Nano Lett.* **2016**, *16*, 800.
[10] L. Protesescu, S. Yakunin, M. I. Bodnarchuk, F. Krieg, R. Caputo, C. H. Hendon, R. X. Yang, A. Walsh, M. V. Kovalenko, *Nano Lett.* **2015**, *15*, 3692.
[11] Q. A. Akkerman, V. D'Innocenzo, S. Accornero, A. Scarpellini, A. Petrozza, M. Prato, L. Manna, *J. Am. Chem. Soc.* **2015**, *137*, 10276.
[12] V. Adinolfi, O. Ouellette, M. I. Saidaminov, G. Walters, A. L. Abdelhady, O. M. Bakr, E. H. Sargent, *Adv. Mater.* **2016**, *28*, 7264.
[13] Y. Yue, Z. Yang, N. Liu, W. Liu, H. Zhang, Y. Ma, C. Yang, J. Su, L. Li, F. Long, Z. Zou, Y. Gao, *ACS Nano* **2016**, *10*, 11249.
[14] S. A. Veldhuis, P. P. Boix, N. Yantara, M. Li, T. C. Sum, N. Mathews, S. G. Mhaisalkar, *Adv. Mater.* **2016**, *28*, 6804.
[15] Z. Zhu, J.-Q. Xu, C.-C. Chueh, H. Liu, Z. a. Li, X. Li, H. Chen, A. K. Y. Jen, *Adv. Mater.* **2016**, 1600027.
[16] D. Bi, C. Yi, J. Luo, J.-D. Décoppet, F. Zhang, S. M. Zakeeruddin, X. Li, A. Hagfeldt, M. Grätzel, *Nat. Energy* **2016**, *1*, 16142.
[17] Y. Liu, Z. Yang, D. Cui, X. Ren, J. Sun, X. Liu, J. Zhang, Q. Wei, H. Fan, F. Yu, X. Zhang, C. Zhao, S. Liu, *Adv. Mater.* **2015**, *27*, 5176.
[18] Z. Lian, Q. Yan, T. Gao, J. Ding, Q. Lv, C. Ning, Q. Li, J.-l. Sun, *J. Am. Chem. Soc.* **2016**, *138*, 9409.
[19] Y. Kutes, Y. Zhou, J. L. Bosse, J. Steffes, N. P. Padture, B. D. Huey, *Nano Lett.* **2016**, *16*, 3434.
[20] B. Ding, L. Gao, L. Liang, Q. Chu, X. Song, Y. Li, G. Yang, B. Fan, M. Wang, C. Li, C. Li, *ACS Appl. Mater. Interfaces* **2016**, *8*, 20067.
[21] F. Zhang, H. Zhong, C. Chen, X.-g. Wu, X. Hu, H. Huang, J. Han, B. Zou, Y. Dong, *ACS Nano* **2015**, *9*, 4533.
[22] D. N. Dirin, L. Protesescu, D. Trummer, I. V. Kochetygov, S. Yakunin, F. Krumeich, N. P. Stadie, M. V. Kovalenko, *Nano Lett.* **2016**, *16*, 5866.
[23] P. K. Nayak, D. T. Moore, B. Wenger, S. Nayak, A. A. Haghighirad, A. Fineberg, N. K. Noel, O. G. Reid, G. Rumbles, P. Kukura, K. A. Vincent, H. J. Snaith, *Nat. Commun.* **2016**, *7*, 13303.
[24] S. Bag, M. F. Durstock, *ACS Appl. Mater. Interfaces* **2016**, *8*, 5053.
[25] M. Saliba, K. W. Tan, H. Sai, D. T. Moore, T. Scott, W. Zhang, L. A. Estroff, U. Wiesner, H. J. Snaith, *J. Phys. Chem. C* **2014**, *118*, 17171.
[26] M. I. Saidaminov, A. L. Abdelhady, B. Murali, E. Alarousu, V. M. Burlakov, W. Peng, I. Dursun, L. Wang, Y. He, G. Maculan, A. Goriely, T. Wu, O. F. Mohammed, O. M. Bakr, *Nat. Commun.* **2015**, *6*, 7586.
[27] J.-J. Li, J.-Y. Ma, J.-S. Hu, D. Wang, L.-J. Wan, *ACS Appl. Mater. Interfaces* **2016**, *8*, 26002.
[28] C. Bi, Y. Shao, Y. Yuan, Z. Xiao, C. Wang, Y. Gao, J. Huang, *J. Mater. Chem. A* **2014**, *2*, 18508.
[29] N. J. Jeon, J. H. Noh, Y. C. Kim, W. S. Yang, S. Ryu, S. I. Seok, *Nat. Mater.* **2014**, *13*, 897.
[30] L. Huang, Z. Hu, J. Xu, K. Zhang, J. Zhang, Y. Zhu, *Sol. Energy Mater. Sol. Cells* **2015**, *141*, 377.
[31] L. Etgar, P. Gao, P. Qin, M. Graetzel, M. K. Nazeeruddin, *J. Mater. Chem. A* **2014**, *2*, 11586.
[32] M. R. Ahmadian-Yazdi, F. Zabihi, M. Habibi, M. Eslamian, *Nanoscale Res. Lett.* **2016**, *11*, 408.
[33] G. Niu, X. Guo, L. Wang, *J. Mater. Chem. A* **2015**, *3*, 8970.
[34] G. E. Eperon, S. N. Habisreutinger, T. Leijtens, B. J. Bruijnaers, J. J. van Franeker, D. W. deQuilettes, S. Pathak, R. J. Sutton, G. Grancini, D. S. Ginger, R. A. J. Janssen, A. Petrozza, H. J. Snaith, *ACS Nano* **2015**, *9*, 9380.
[35] G. Wang, D. Li, H.-C. Cheng, Y. Li, C.-Y. Chen, A. Yin, Z. Zhao, Z. Lin, H. Wu, Q. He, M. Ding, Y. Liu, Y. Huang, X. Duan, *Sci. Adv.* **2015**, *1*, e1500613.
[36] L. Niu, X. Liu, C. Cong, C. Wu, D. Wu, T. R. Chang, H. Wang, Q. Zeng, J. Zhou, X. Wang, W. Fu, P. Yu, Q. Fu, S. Najmaei, Z. Zhang, B. I. Yakobson, B. K. Tay, W. Zhou, H. T. Jeng, H. Lin, T. C. Sum, C. Jin, H. He, T. Yu, Z. Liu, *Adv. Mater.* **2015**, *27*, 7800.
[37] M. Spina, E. Bonvin, A. Sienkiewicz, B. Náfrádi, L. Forró, E. Horváth, *Sci. Rep.* **2016**, *6*, 19834.
[38] J. Feng, X. Yan, Y. Zhang, X. Wang, Y. Wu, B. Su, H. Fu, L. Jiang, *Adv. Mater.* **2016**, *28*, 3732.
[39] T. Jeon, H. M. Jin, S. H. Lee, J. M. Lee, H. I. Park, M. K. Kim, K. J. Lee, B. Shin, S. O. Kim, *ACS Nano* **2016**, *10*, 7907.
[40] S. S. Chou, B. S. Swartzentruber, M. T. Janish, K. C. Meyer, L. B. Biedermann, S. Okur, D. B. Burckel, C. B. Carter, B. Kaehr, *J. Phys. Chem. Lett.* **2016**, *7*, 3736.
[41] J. Shamsi, A. L. Abdelhady, S. Accornero, M. Arciniegas, L. Goldoni, A. R. S. Kandada, A. Petrozza, L. Manna, *ACS Energy Lett.* **2016**, *1*, 1042.
[42] S. M. Eaton, H. Zhang, P. R. Herman, F. Yoshino, L. Shah, J. Bovatsek, A. Y. Arai, *Opt. Express* **2005**, *13*, 4708.
[43] F. Meng, S. A. Morin, A. Forticaux, S. Jin, *Acc. Chem. Res.* **2013**, *46*, 1616.
[44] A. J. Alexander, *Nat. Photonics* **2016**, *10*, 694.
[45] B. Brunetti, C. Cavallo, A. Ciccioli, G. Gigli, A. Latini, *Sci. Rep.* **2016**, *6*, 31896.
[46] S. Yakunin, D. N. Dirin, Y. Shynkarenko, V. Morad, I. Cherniukh, O. Nazarenko, D. Kreil, T. Nauser, M. V. Kovalenko, *Nat. Photonics* **2016**, *10*, 585.
[47] Z.-Y. Zhang, H.-Y. Wang, Y.-X. Zhang, K.-J. Li, X.-P. Zhan, B.-R. Gao, Q.-D. Chen, H.-B. Sun, *Phys. Chem. Chem. Phys.* **2017**, *19*, 2217.
[48] P. Tyagi, S. M. Arveson, W. A. Tisdale, *J. Phys. Chem. Lett.* **2015**, *6*, 1911.
[49] R. G. Forbes, *Appl. Phys. Lett.* **2008**, *92*, 193105.
[50] Y. Zhang, K. Miszta, L. Manna, E. Di Fabrizio, R. Krahne, *Nanoscale* **2013**, *5*, 7596.
[51] C. A. Leatherdale, C. R. Kagan, N. Y. Morgan, S. A. Empedocles, M. A. Kastner, M. G. Bawendi, *Phys. Rev. B.* **2000**, *62*, 2669.
[52] A. Persano, M. De Giorgi, A. Fiore, R. Cingolani, L. Manna, A. Cola, R. Krahne, *ACS Nano* **2010**, *4*, 1646.

Q5

Q1 APT to AU: Please provide the highest academic title (either Dr. or Prof.) for all authors, where applicable.

Q2 APT to AU: Please define all acronyms, such as, MAI, HX, DAPI, FITC, TRITC, NIR, CSM at their first appearance in the abstract, text, and table of contents, respectively. Only expanded forms are allowed if the elements are cited only once in the article.

Q3 APT to AU: If you have not returned the color cost confirmation form already, please email the completed form to the editorial office when you submit your proof corrections. This will confirm that you are willing to support the cost for color publication of the figures. Details about our color policies and a link to the form were included with your acceptance email. If you wish for your figures to be presented in greyscale, please email the editorial office to confirm this.

Q4 APT to AU: 'Author Contributions' and 'Notes' have been set under Acknowledgements section. Please verify.

Q5 APT to AU: Please provide the volume number in ref. (15), if applicable.